Journal of *Marine Science and Engineering*

MDPI

Article

CNN-GRU-ATT Method for Resistivity Logging Curve Reconstruction and Fluid Property Identification in Marine Carbonate Reservoirs

Jianhong Guo [1], Hengyang Lv [1], Qing Zhao [1,2], Yuxin Yang [3], Zuomin Zhu [1] and Zhansong Zhang [1,*]

[1] Key Laboratory of Exploration Technologies for Oil and Gas Resources, Ministry of Education, Yangtze University, Wuhan 430100, China; 2022730024@yangtzeu.edu.cn (J.G.); 2023710429@yangtzeu.edu.cn (H.L.); 2021710322@yangtzeu.edu.cn (Q.Z.)
[2] Seventh Oil Production Plant, Changqing Oilfield, Qingyang 745000, China
[3] Hubei Cooperative Innovation Center of Unconventional Oil & Gas, Yangtze University, Wuhan 430100, China
* Correspondence: zhangzhs@yangtzeu.edu.cn

Abstract: Geophysical logging curves are crucial for oil and gas field exploration and development, and curve reconstruction techniques are a key focus of research in this field. This study proposes an inversion model for deep resistivity curves in marine carbonate reservoirs, specifically the Mishrif Formation of the Halfaya Field, by integrating a deep learning model called CNN-GRU-ATT, which combines Convolutional Neural Networks (CNN), Gated Recurrent Units (GRU), and the Attention Mechanism (ATT). Using logging data from the marine carbonate oil layers, the reconstructed deep resistivity curve is compared with actual measurements to determine reservoir fluid properties. The results demonstrate the effectiveness of the CNN-GRU-ATT model in accurately reconstructing deep resistivity curves for carbonate reservoirs within the Mishrif Formation. Notably, the model outperforms alternative methods such as CNN-GRU, GRU, Long Short-Term Memory (LSTM), Multiple Regression, and Random Forest in new wells, exhibiting high accuracy and robust generalization capabilities. In practical applications, the response of the inverted deep resistivity curve can be utilized to identify the reservoir water cut. Specifically, when the model-inverted curve exhibits a higher response compared to the measured curve, it indicates the presence of reservoir water. Additionally, a stable relative position between the two curves suggests the presence of a water layer. Utilizing this method, the oil–water transition zone can be accurately delineated, achieving a fluid property identification accuracy of 93.14%. This study not only introduces a novel curve reconstruction method but also presents a precise approach to identifying reservoir fluid properties. These findings establish a solid technical foundation for decision-making support in oilfield development.

Keywords: well-log reconstruction; CNN-GRU-ATT method; reservoir fluid property identification; marine carbonate reservoir; Mishrif Formation

check for updates

Academic Editor: Atilla Incecik

Received: 14 January 2025
Revised: 6 February 2025
Accepted: 9 February 2025
Published: 12 February 2025

Citation: Guo, J.; Lv, H.; Zhao, Q.; Yang, Y.; Zhu, Z.; Zhang, Z. CNN-GRU-ATT Method for Resistivity Logging Curve Reconstruction and Fluid Property Identification in Marine Carbonate Reservoirs. *J. Mar. Sci. Eng.* **2025**, *13*, 331. https://doi.org/10.3390/jmse13020331

Copyright: © 2025 by the authors. Licensee MDPI, Basel, Switzerland. This article is an open access article distributed under the terms and conditions of the Creative Commons Attribution (CC BY) license (https://creativecommons.org/licenses/by/4.0/).

1. Introduction

Geophysical logging technology plays a crucial role in the exploration of oil and gas resources [1,2]. Utilizing geophysical logging instruments, parameters such as resistivity, acoustic velocity, density, and natural gamma of rocks and reservoirs can be collected [3,4]. These parameters are used for lithology identification, and calculation of reservoir porosity, permeability, and saturation, providing the data foundation for subsequent oil and gas reservoir volume assessment and exploration and development planning [5–7].

In practical exploration, geophysical logging data collected by logging instruments are often affected by multiple factors, such as instrument malfunction, operational errors, borehole environmental interference [8–10], etc. These factors are coupled and ultimately affect the quality of logging curve collection, potentially leading to data loss or degradation. Therefore, reconstructing missing logging curves, i.e., reconstructing uncollected logging data, is one of the fundamental tasks to ensure the normal progress of subsequent reservoir parameter evaluation work [11]. Early logging curve reconstruction techniques were mostly based on statistical methods [12], which mainly utilized statistical principles to predict missing data based on the statistical characteristics of existing data distributions, including linear interpolation, polynomial interpolation, spline interpolation, etc. Subsequently, physics-based methods based on rock physics models were also applied. These methods consider the relationship between logging curves and rock's physical properties [13]. However, the accuracy of such methods is relatively low and may affect the calculation of subsequent quantitative parameters [14]. With the increasing demand for the accuracy of inversion curves and the development of machine learning methods, more and more scholars have begun to attempt to apply them to logging curve reconstruction, such as multivariate regression, Back-Propagation Neural Network (BPNN), Support Vector Machine Regression (SVR), eXtreme Gradient Boosting (XGB), etc., which have been proven to be effective [15–17]. Different from building models for logging curves and core parameters, obtaining core parameters requires sampling and experimental determination, which consumes a high amount of time and economic cost and is limited in quantity. When reconstructing logging curves, there are richer sample quantities. Additionally, considering that deep learning methods have stronger data representation capabilities and logging data are related to reservoir depth changes, deep learning methods have also been applied in the field of logging curve reconstruction. Zhang et al. [18] proposed a logging curve reconstruction method employing the Long Short-Term Memory (LSTM) algorithm. Their approach integrates LSTM neural networks with formation lithology indexes for data filtering and model training. They ultimately achieved an efficient and accurate logging curve reconstruction model through particle swarm optimization. Wang et al. [19] investigated the application of Gated Recurrent Unit (GRU) neural networks for logging curve reconstruction. Through trial calculations on actual data, they demonstrated the promising results achieved by the GRU network model, offering a novel avenue for logging curve reconstruction. Exploring further options, Lin et al. [20] presented a deep learning framework based on the Transformer architecture to effectively reconstruct missing well-logging data in the Sichuan Basin. Similarly, Ren et al. [21] developed a time series regression model that predicted missing well-logging data by incorporating lithology information as additional geological input. Denoising was achieved using Discrete Wavelet Transform (DWT), resulting in accurate restoration of missing well-logging data. For the reconstruction of missing shear wave slowness (DTS) data in shale gas reservoirs, Guo et al. [22] proposed a deep learning model utilizing Generative Adversarial Networks (GAN). Their method involved employing LSTM as generators to capture the overall trend of logging data and generate pseudo-DTS sequences. Additionally, one-dimensional Convolutional Neural Networks (1DCNN) acted as discriminators to identify local data details and determine the authenticity of DTS sequences. Experimental validation using actual data confirmed the effectiveness of their approach. The aforementioned studies showcase various approaches and techniques for reconstructing missing well-logging data in different geological contexts.

Previous curve reconstruction research mainly focuses on reconstructing DTS curves or porosity series logging curves, and there are few studies on the reconstruction of resistivity logging curves. The response of resistivity logging curves is influenced by various factors, such as surrounding rock pressure, temperature, reservoir pore space type, conductive min-

erals, reservoir factors, as well as time differences between drilling and logging, instrument differences, and other construction factors [23–25]. Among them, the influence of reservoir fluid properties on resistivity is significant. The comprehensive factors mentioned above make the actual response of resistivity logging curves extremely complex. The difference in resistivity of oil and gas reservoirs under different geological backgrounds is huge. In the Mishrif Formation in the Middle East, oil layer resistivity can range from as low as 2 mD to over 2000 mD, posing challenges in resistivity curve reconstruction. However, these curves are vital for quantitatively interpreting logging data, such as assessing reservoir water saturation and distinguishing water from oil/gas layers [26–28]. While the difference in resistivity response is commonly used to identify oil and water layers in practical oilfield operations, accurately quantifying this response, particularly in water-containing reservoirs, remains a technical challenge. This ambiguity in determining the resistivity decrease range hampers the precise positioning of the transition zone, impacting the selection of perforation intervals.

To address the challenges, this paper focuses on the marine carbonate Mishrif reservoir in the Middle East, departing from previous approaches to logging curve reconstruction. Leveraging trial oil data and production data from production wells, the method employs the logging curve response of pure oil reservoirs as training samples, with the deepest resistivity curve (deep resistivity RD) as the prediction target and other curves and derived parameters as feature vectors. A novel approach, the CNN-GRU-ATT method, is proposed, integrating Convolutional Neural Networks (CNN), GRU, and Attention Mechanism (ATT), to construct a theoretical oil layer resistivity curve. By comparing this constructed curve with resistivity curves measured by actual logging instruments, reservoir fluid properties are determined and validated through production and testing. This method introduces a new algorithm for logging curve reconstruction and offers a model construction approach that effectively identifies reservoir fluid properties and accurately determines the oil–water interface in the Mishrif Formation during practical engineering applications, thus demonstrating significant engineering value.

2. Geological Overview

2.1. Geological Situation

The Mishrif Formation, situated within the Halfaya oilfield (see Figure 1), is structurally positioned in the foredeep of the Mesopotamian Basin, forming a broad northwest–southeast trending anticline [29,30]. This Upper Cretaceous formation is predominantly found along the northeastern edge of the Arabian Plate, east of the Zagros Fold-Thrust Belt. With a thickness of up to 400 m, it is overlain by the Khasib Formation and underlain by the Runaila Formation [31,32].

Comprising three main sections, namely MA, MB, and MC, the Mishrif Formation further subdivides the MB section into MB1 and MB2. Predominantly composed of bioclastic granular limestone, bioclastic micritic limestone, and granular limestone (as depicted in Figure 1), it serves as a pure porous limestone reservoir. Previous literature identifies calcite as the primary mineral, constituting over 90% of the formation [33]. The reservoir exhibits diverse and complex pore space types, primarily matrix micropores and moldic pores. Porosity levels range from 4% to 35%, averaging at 17.15%. Permeability varies widely, spanning from 0.01 millidarcies (md) to 1100 md, with an average of 20.58 md, indicating pronounced reservoir heterogeneity [34].

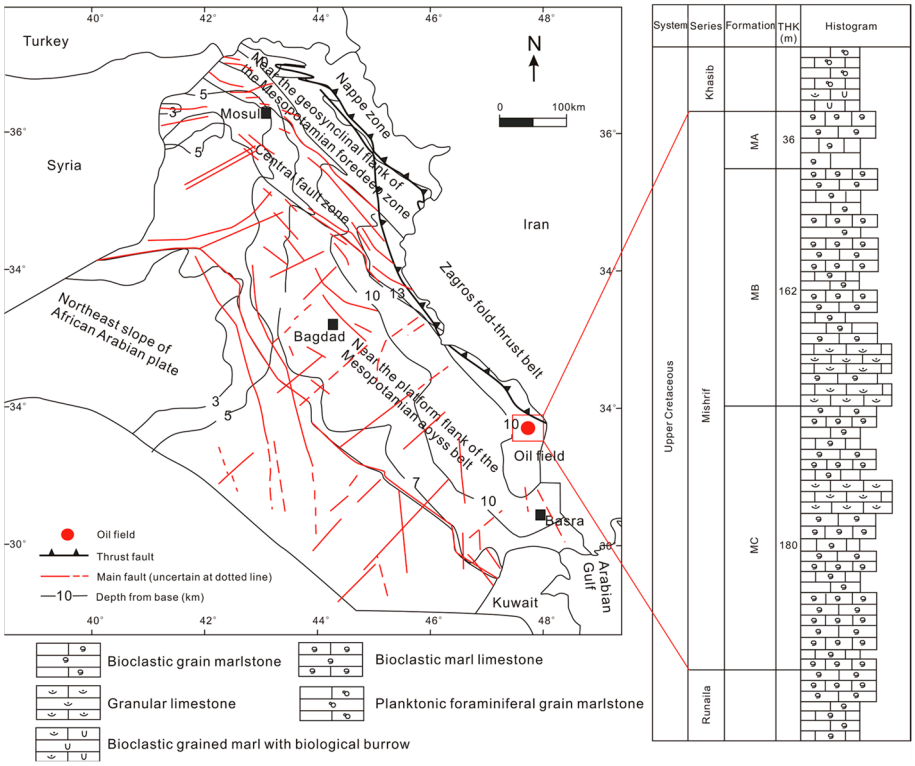


Figure 1. The location of the study area in Halfaya oilfield and the lithologic column diagram of Mishrif Formation [34].

In the marine environment, the accumulation and decomposition of organisms such as coral reefs and calcareous algae, along with changes in the chemical conditions of the water, contribute to the formation of diversified pore structures. According to petrographic casting thin section (CTS) analysis, primary pores mainly include intercrystalline and intergranular pores (Figure 2b). In contrast, secondary pores are predominantly moldic pores (Figure 2a), with fossil-related pores and dissolution pores also being present. In a few samples, microfractures are observed, and within some thin sections, secondary calcite crystals of various sizes are visible within large pores. Some rock samples show the development of dissolution pores and cavities (Figure 2c); however, dissolution pores and cavities are relatively underdeveloped overall. Scanning electron microscope (SEM) observations reveal that pyrite fragments display distinct bacterial filaments, with intercrystalline pores associated with the microcrystalline matrix and pyrite fragments (Figure 2d, green arrows). The macropores include particle-related intragranular pores and dissolution pores related to bright calcite crystals (Figure 2d). In microcrystalline limestone containing foraminifera and mollusk shell fragments, intragranular pores associated with fossils and intercrystalline pores related to the microcrystalline matrix are developed, as well as intercrystalline pores associated with recrystallized fossils (Figure 2e, red arrows). As dissolution intensifies, intragranular dissolution pores expand and form moldic pores. Some particles retain thin films of chlorite (Figure 2f), with the key role of mixed seawater or freshwater leaching during the syn-depositional period in generating intragranular dissolution pores or moldic pores. In deep-water, low-energy environments, the decay of planktonic and benthic foraminiferal skeletons or shells after deposition leads to abundant primary biocavities. The pore types mainly include biocavities and intercrystalline/intercrystalline dissolution pores, forming a mesoporous–microporous combination (Figure 2g). Irregularly curved, filamentous illite–smectite interlayer assemblages, resembling a honeycomb structure, fill intergranular pores with bioclastic debris, developing intergranular dissolution pores (Figure 2h, yellow arrows). The hydration expansion characteristics of this material cause a

reservoir water sensitivity effect, blocking pore throats and leading to an increase in bound water saturation. Book-like, flaky, and worm-like kaolinite microaggregates fill parts of the microcrystalline matrix, forming intercrystalline pores (Figure 2i), and the authigenic kaolinite cementation along with secondary dissolution cavities indicates the presence of acidic fluids.

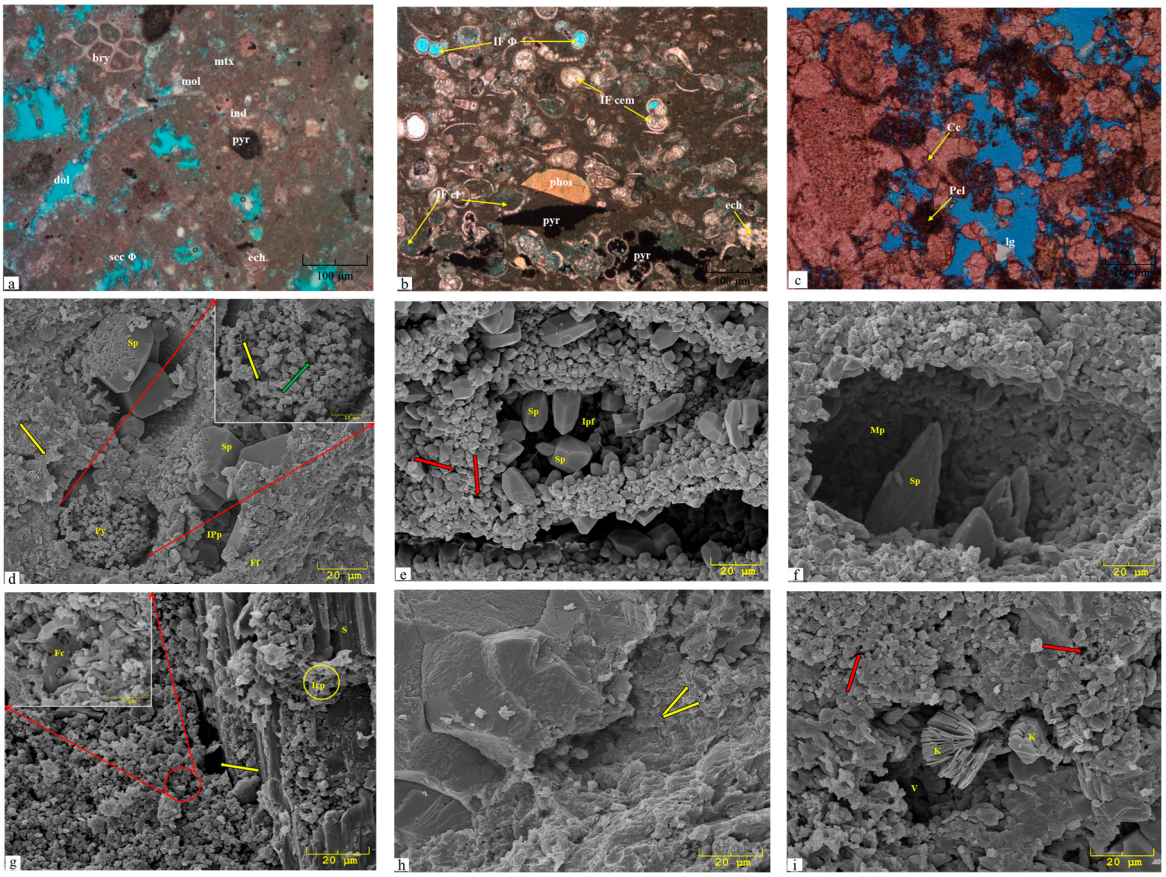


Figure 2. Micro- and nano-scale pore types in the bioclastic limestone of the Mishrif Formation: (**a**) dissolution pores and moldic pores, CTS; (**b**) intergranular pores and biocavities, CTS; (**c**) intercrystalline pores, matrix pores, and dissolution pores, CTS; (**d**) intragranular dissolution pores and biocavities, SEM; (**e**) primary intragranular pores, SEM; (**f**) moldic pores and dissolution pores, SEM; (**g**) matrix micropores, SEM; (**h**) illite–smectite mixed-layer intergranular pores, SEM; (**i**) kaolinite intercrystalline pores, SEM.

2.2. The Equipment Use and Feasibility Evaluation of the Study Area

The response of resistivity logging curves in oil fields is influenced by multiple factors, and differences in resistivity logging instruments may also affect the results. In the study area, resistivity logging curves from boreholes were obtained using two types of instruments: the Dual Laterolog Resistivity Tool (DLL) from Great Wall Drilling Company, Beijing, China, and the Array Laterolog Resistivity Tool (ALRT) from Schlumberger, Houston, TX, USA. To ensure that the differences between the two instruments do not significantly impact the accuracy of the resistivity inversion model, it is necessary to compare the measurement effects of these two instruments.

Two wells were selected, which are close in proximity and have similar drilling and logging times, ensuring consistent geological backgrounds. The locations of these wells are indicated by red circles in Figure 3a. Figure 3b,c present the logging curves of these two wells. In these figures, the first track represents depth, the second track represents stratigraphy, the third track records the lithology logging curves (GR, SP, and CAL curves),

the fourth track shows the porosity logging curves (three porosity curves: CN, DEN, and DT), and the fifth track displays the resistivity curves with the maximum detection depth (true formation resistivity curves). Well WD1 (Figure 3b) used Schlumberger's ALRT, while Well WD2 (Figure 3c) used Great Wall Drilling's DLL. The corresponding instrument schematic diagrams are shown in Figure 3d,e. A–A′ represents the guard or return electrodes, and M–M′ represents the paired monitoring electrodes. By changing the emission guard current electrode and controlling the focusing conditions, the detection range of the two instruments can be altered. Figure 3f illustrates the current schematic at the maximum detection range. The blue line represents the guard electrode current line, and the red line represents the main electrode current line. Under the strong constraint of the guard electrode current line, the deep detection main electrode current line is well focused and penetrates vertically into the deep formation, achieving the farthest detection depth. Changing the guard electrode weakens the constraint on the guard electrode current line, causing the shallow detection main electrode current line to have a general focusing effect, which gradually diverges after penetrating a certain depth into the formation (Figure 3g). The DLL has one deep and one shallow detection range, while the ALRT, with more electrodes, can detect resistivity at different radial depths.

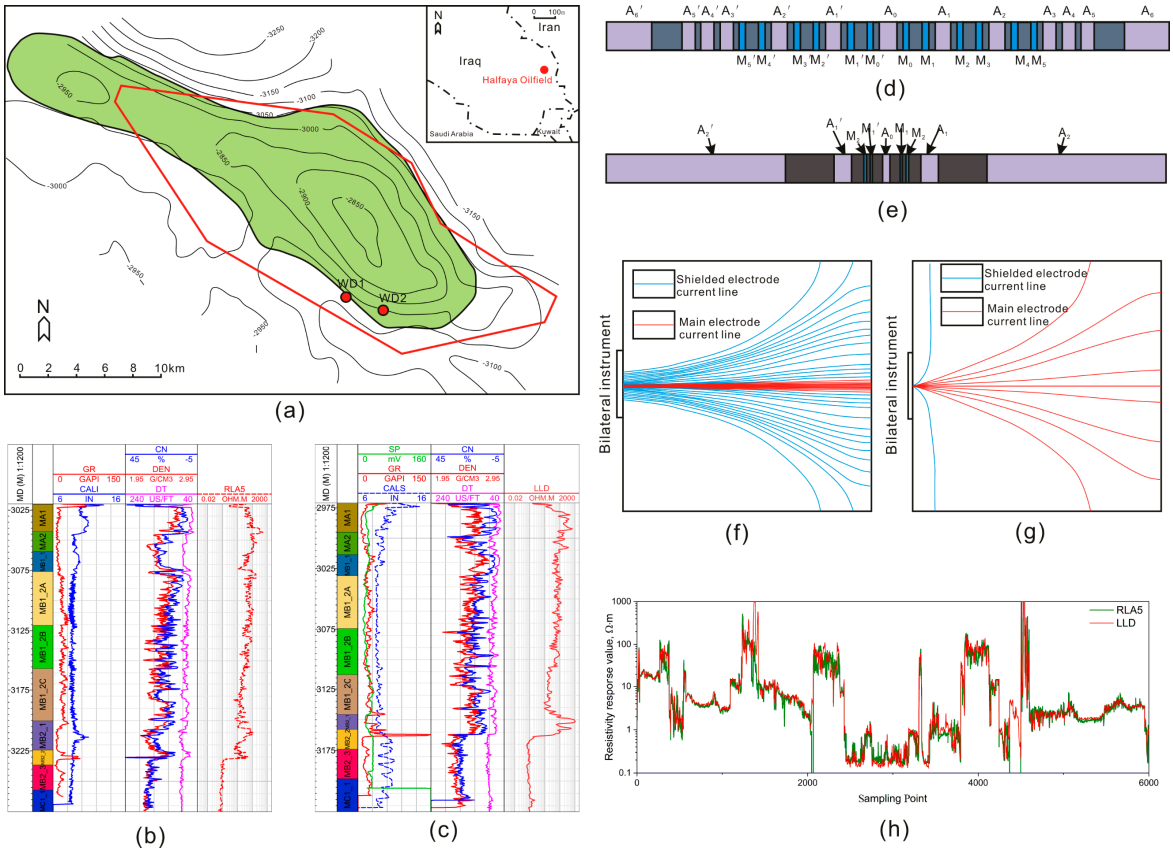


Figure 3. Fundamental data validation diagram: (**a**) well location maps of two wells with similar distances and measured by different instruments; (**b**) logging curves of WD1 well measured by ALRT instrument; (**c**) logging curves of WD2 well measured by DLL instrument; (**d**) the schematic diagram of the structure of the ALRT instrument and the schematic diagram of the relative position of the electrode; (**e**) the structure schematic diagram of the DLL instrument and the schematic diagram of the relative position of the electrode; (**f**) current flow diagram in deep resistivity measurement; (**g**) current flow diagram for shallow resistivity measurement; (**h**) WD1 well and WD2 well resistivity contrast diagram of the same horizon.

Considering that this study focuses on the deepest detection logging curves, we compared the RLA5 curve from Well-WD1 with the LLD curve from Well-WD2. The LLD curve from Well WD2 was resampled and interpolated to align with the same stratigraphic level as the sampling scale of Well WD1. The comparison of the two resistivity curves is shown in Figure 3h, indicating that the resistivity curves measured by both instruments at the maximum detection depth show consistent trends at the same stratigraphic level under the same geological background. This demonstrates that the deep resistivity responses measured by both instruments are consistent and reliable, confirming that the fundamental data of this study are reliable and feasible.

3. Method Principle and Process

In this study, a deep learning algorithm is used to reconstruct the true formation resistivity curves of oil reservoirs. The algorithm is based on CNN, GRU, and the ATT, forming a CNN-GRU-ATT network model [35].

3.1. CNN Algorithm

CNN is a commonly used deep learning model, primarily consisting of convolutional layers, pooling layers, and fully connected layers, as shown in Figure 3. The convolutional layers extract features from input data using multiple filters, while the pooling layers enhance computational efficiency by reducing dimensionality, and retaining key features [36]. CNNs come in various structural forms, including one-dimensional (1D), two-dimensional (2D), and three-dimensional (3D) configurations. Since well-logging curve prediction requires handling multi-sequence input data with coupled relationships between curves, this study utilizes a one-dimensional convolutional neural network (1D CNN) for modeling. Compared to traditional multilayer perceptrons and other neural networks, CNNs significantly reduce model complexity and improve generalization ability by using local connections and weight sharing, while effectively capturing the local correlations in well-logging data [37]. CNNs abstract the features of the input data layer by layer, while preserving its spatial topology, enabling better handling of the topological relationships inherent in the well-logging data. In this study, zero padding is applied at the edges to ensure that the size and structural order of the data remain consistent after convolution, facilitating the subsequent capture of temporal dynamic features by the GRU.

Through a sliding window approach, this vector is segmented into feature maps, each with dimensions of M × N. Here, M represents the hyperparameter for the time step, while N signifies the number of input logging curves. Each feature map is then fed into the CNN model (see Figure 4), which performs convolution operations to capture features across multiple variables in the spatial topology, as illustrated in Figure 5.

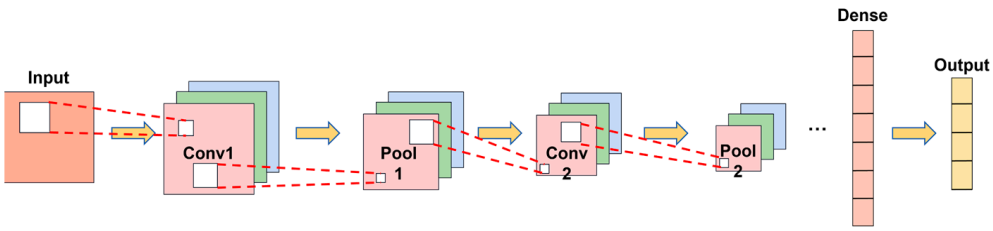


Figure 4. Basic structure of CNN.

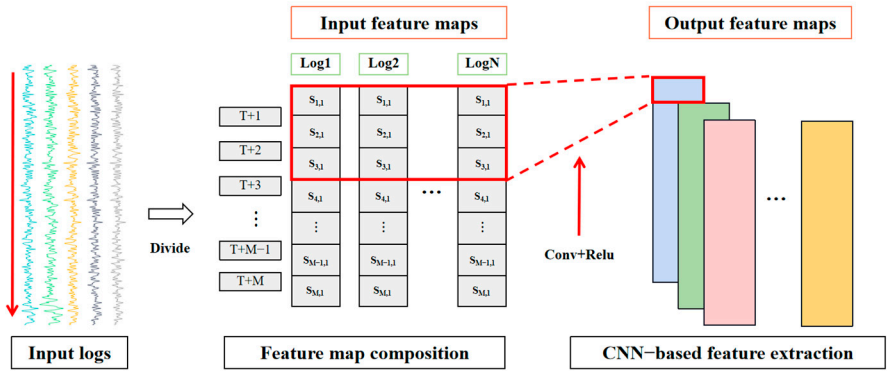


Figure 5. Feature combination and extraction based on CNN.

3.2. GRU Algorithm

The Gated Recurrent Unit (GRU) is a variant of the Recurrent Neural Network (RNN) that addresses the vanishing gradient problem encountered by traditional RNNs when processing long sequence data [38]. Although the chain structure of RNNs is effective for sequence modeling, the single memory unit limits the transmission of long-term dependencies, especially in deep networks. GRU enhances memory capacity by introducing two gating mechanisms: the reset gate and the update gate. The reset gate determines whether to retain or discard previous information, while the update gate controls the degree of forgetfulness, allowing the model to adapt to long-term dependencies [39]. Compared to LSTM networks, the GRU has a simpler structure and lower computational overhead while achieving similar performance [40]. The basic structure of the GRU network is shown in Figure 6, and the forward propagation is described by Equations (1)–(4).

$$r_t = \sigma(W_r x_t + U_r h_{t-1} + b_r) \tag{1}$$

$$z_t = \sigma(W_z x_t + U_z h_{t-1} + b_z) \tag{2}$$

$$\overline{h}_t = \tanh(W_h x_t + U_h(r_t \odot h_{t-1})x + b_h) \tag{3}$$

$$h_t = z_t \odot h_{t-1} + (1 - z_t) \odot \overline{h}_t \tag{4}$$

where x_t is the input at time t; h_t and h_{t-1} are the hidden layer outputs at time t and $t-1$, respectively, and $\overline{h_t}$ is the candidate hidden state. z_t is the update gate, and r_t is the reset gate. U_r, U_z, U_h, W_r, W_z, W_h, b_r, b_z, b_h are the weight vectors, weight matrices, and biases for the reset gate, update gate, and candidate hidden state, respectively. σ is the sigmoid function, and tanh is the activation function.

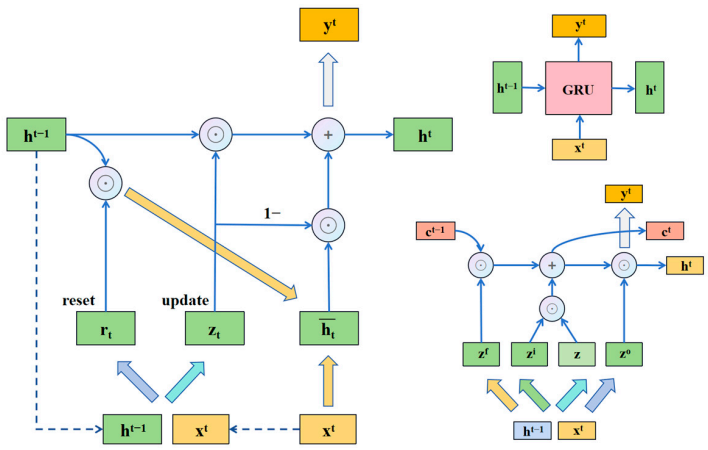


Figure 6. Basic structure of GRU network.

3.3. Attention Mechanism

The ATT enables the model to assign varying importance weights to distinct sections of the input sequence or dataset. By automatically focusing on relevant information in the input, the model can learn and process complex relationships more effectively, improving performance and generalization capability [41]. The structure of the ATT is shown in Figure 7, and the computation formulas are given by Equations (5)–(7).

$$h_i = \alpha(x_i) \tag{5}$$

$$\alpha_i = Softmax(h_i) = \frac{\exp(h_i)}{\sum_{i=1}^{N} \exp(h_i)} \tag{6}$$

$$y = \sum_{i}^{N} \alpha_i h_i \tag{7}$$

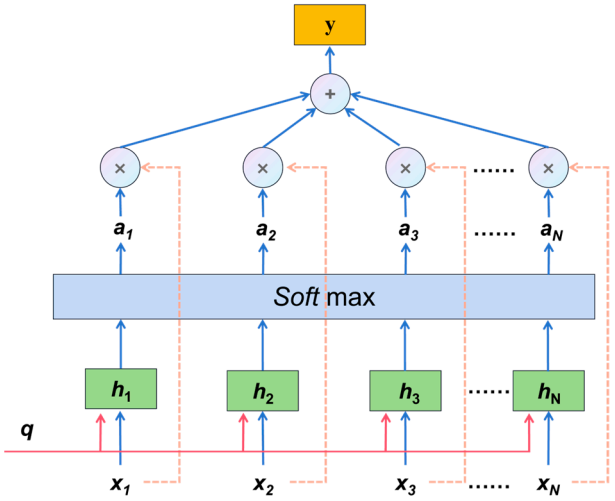


Figure 7. Attention Mechanism structure.

The vectors $x_1, x_2, \ldots, x_n$ represent the hidden layer outputs of the GRU at each time step, and $h_1, h_2, \ldots, h_n$ are their corresponding weight coefficients; $a_1, a_2, \ldots, a_n$ are the normalized weight coefficient of Soft max; y is the output value obtained by weighted summation, and q is the query vector.

3.4. CNN-GRU-ATT Model

This paper proposes a CNN-GRU-ATT-based neural network model that fully leverages its high nonlinearity, adaptability, and self-learning capabilities in nonlinear dynamic modeling for the prediction of multi-mineral component contents. The model integrates the advantages of CNN, GRU, and the Attention Mechanism, capitalizing on their strengths in their respective domains. Specifically, CNN is used to extract spatial features, GRU captures temporal sequence features, and the Attention Mechanism assigns higher weights to key features, further optimizing the model's predictive performance. The CNN-GRU-ATT model combines the structural advantages of each network, compensating for the limitations of individual models. This approach not only reduces training time but also accelerates network convergence, thereby enhancing overall performance.

Additionally, the model employs Dropout and early stopping strategies, proposed by Srivastava et al. [42]. During each training process, the Dropout layer randomly drops certain input feature weights with a specified probability, enhancing the model's general-

ization ability and robustness by reducing dependency on specific inputs. Early stopping halts training when the training error no longer decreases after a set number of epochs.

The neural network model in Figure 8 consists of essential components like input layers, convolutional layers, max-pooling layers, Dropout layers, GRU layers, Attention layers, fully connected layers, and an output layer. These components work together to achieve optimal performance. Data preprocessing precedes the convolutional layers to extract relevant features, followed by max-pooling layers to reduce data dimensionality. Dropout layers are then applied to enhance generalization. A flattened layer prepares the data for subsequent GRU layers, effectively capturing temporal dependencies in time series data. This architecture allows the model to comprehensively process input data and leverage various techniques for optimized performance. Finally, the Attention layer processes the sequence data, focusing on input features relevant to the current context, followed by two fully connected layers for regression tasks.

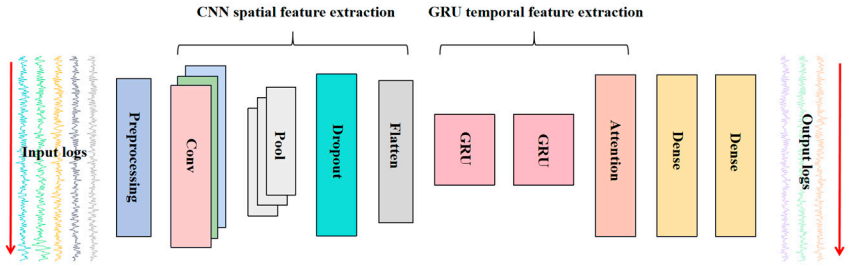


Figure 8. CNN-GRU-Attention Model network structure.

After determining the model network structure, the experimental process of this study is shown in Figure 9:

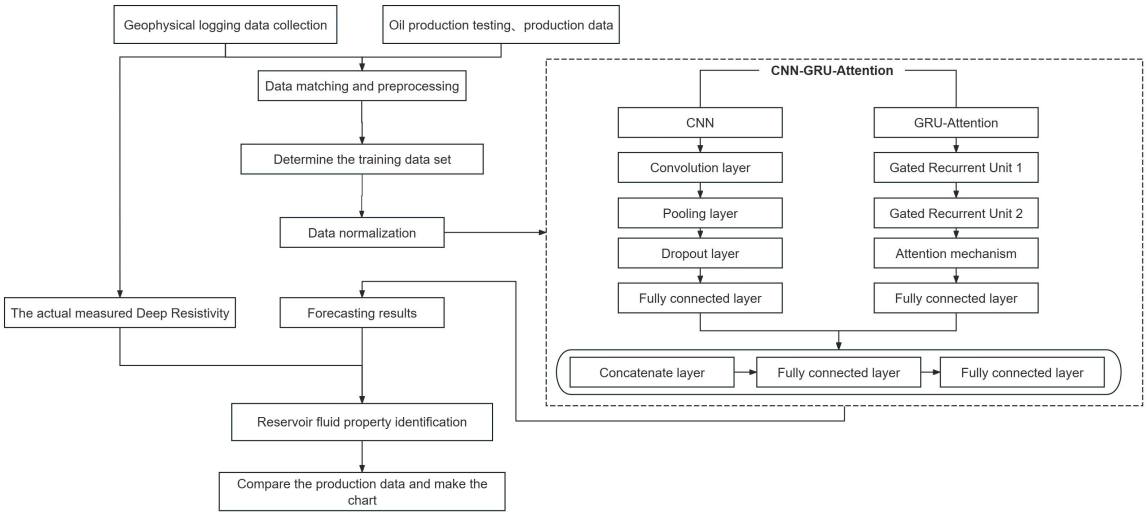


Figure 9. Flowchart of the research in this paper.

First, data collection and production data organization are conducted, including collecting geophysical logging data, determining the oil reservoir sections based on test results and production results, and calculating derived parameters.

The data used for model training are then normalized, and the CNN-GRU-ATT method is used to construct the deep resistivity inversion curves of the oil reservoir.

The performance of the trained model is assessed by evaluating it on validation data and new wells, employing appropriate metrics for evaluation.

In the application of the model, the inverted resistivity is compared to the measured deep resistivity to ascertain the properties of the reservoir fluids.

4. Model Construction Process and Results

4.1. Logging Curve Selection

In the data preprocessing phase, the treatment of missing data in this study differs from traditional reservoir parameter evaluation models. Traditional models typically rely on core samples, which are limited in number, generally not exceeding 1000 sets. In contrast, the well-log curve reconstruction in this study provides a richer data resource, with data from a single layer of each well often exceeding 1000 sets. Therefore, missing data have minimal impact on model construction, and wells with significantly missing data are excluded from the modeling process.

Regarding noise treatment, well-log curves typically contain noise due to factors such as borehole environment, instrument precision, and on-site human factors. Previous studies have shown that such noise cannot be addressed in isolation. Therefore, we rely on manual screening to remove obvious anomalous responses, particularly those with abnormally high values, ensuring the validity and accuracy of the data.

Before constructing the deep resistivity inversion model of the oil reservoir, it is essential to determine the curves involved in the model construction. Based on the borehole data from the study area, most boreholes include natural gamma curves, caliper curves, and triple porosity series curves (DT curve, DEN curve, and CN curve). Due to differences in instruments, the number of resistivity series curves typically ranges from 3 to 5. Since the deep resistivity curve is the inversion target, resistivity series curves are not included in the model construction. Additionally, calculated parameters such as porosity and constructed features like the triple porosity ratio and triple porosity difference (Equations (8) and (9)) can be used as feature vectors to enrich the model.

$$\phi_D = \phi_{da} + \phi_{sa} - 2 \times \phi_{na} \tag{8}$$

$$\phi_R = \frac{\phi_{da} \times \phi_{sa}}{{\phi_{na}}^2} \tag{9}$$

In Equations (8) and (9), ϕ_D represents the difference in porosity, expressed in porosity units (pu); ϕ_R denotes the dimensionless ratio of porosities; ϕ_{da} stands for the apparent density porosity; ϕ_{na} denotes the apparent neutron porosity; and ϕ_{na} represents the apparent sonic porosity. All units are in porosity units (pu), calculated using log data combined with volumetric models.

The correlation analysis between log curves and the depth resistivity measured by each instrument, including the derived parameters, is conducted. Table 1 presents the *Pearson index* of the curves.

Table 1. Correlation between curve response and deep resistivity.

Pearson	AC μs/ft	CN Pu	DEN g/cm^3	GR API	ϕ Pu	ϕ_D Pu	ϕ_R
RD(LLD/RLA5) $\Omega \cdot m$	−0.31	−0.37	0.28	−0.49	−0.34	0.40	0.38

Combining the analysis of the data in Table 1, a negative correlation between porosity and resistivity is observed. Utilizing data from rock electrical experiments, characterization is performed. For the collected 69 rock core samples, when fully saturated with water, the relationship between core porosity and rock resistivity is statistically analyzed (Figure 10a). The analysis indicates that with an increase in porosity under single-fluid conditions, the rock resistivity decreases, corresponding to the decrease in compensated density logging response in Table 1. The increase in sonic transit time logging response and compensated

neutron porosity typically indicates an increase in reservoir porosity. This also explains the correlation between the three porosity curves and deep resistivity. However, due to the actual oil-bearing reservoirs not being fully saturated with water and various factors influencing the determination of the actual deep resistivity response, the porosity logging series curves and calculated porosity do not exhibit a simple linear relationship with the resistivity logging response.

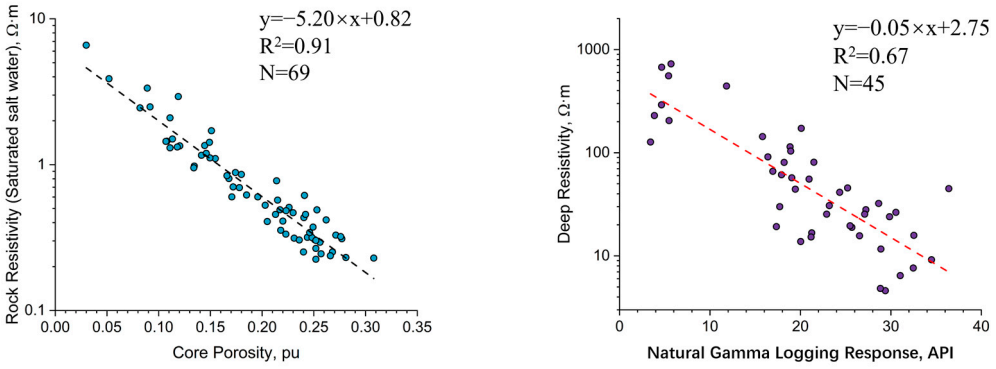


Figure 10. Rendezvous plots between experimental parameters: (**a**) porosity vs. rock resistivity rendezvous plot in water-saturated core samples; (**b**) correlation between GR response and RD response.

By comparing the relationship between GR and RD in the oil-bearing section, it is evident that an increase in GR logging response corresponds to a decrease in resistivity (Figure 10b). The phenomenon can be ascribed to the reservoir's higher clay mineral content, indicated by the elevated natural gamma response. In the study area, the prevalent clay minerals, such as illite and montmorillonite, possess conductive properties. Consequently, the rise in clay content leads to a reduction in resistivity response.

In summary, this study focuses on porosity logging series curves and natural gamma logging curves. The derived parameters primarily include calculated porosity parameters, three porosity differences, and three porosity ratios. Table 2 presents randomly selected data samples, featuring well numbers, sampling point depths, characteristic curves, and the corresponding RD target curve.

Table 2. Samples used to construct the inversion model.

Well No.	Depth m	AC μs/ft	CN Pu	DEN g/cm^3	GR API	ϕ Pu	ϕ_D Pu	ϕ_R	RD Ω·m
M-001	2881.98	74.28	0.16	2.39	20.19	0.12	0.05	1.34	56.63
M-001	2885.08	69.88	0.06	2.48	24.23	0.07	0.17	5.48	43.28
M-001	2885.18	70.40	0.06	2.47	23.96	0.06	0.18	5.86	42.63
⋮	⋮	⋮	⋮	⋮	⋮	⋮	⋮	⋮	⋮
M-047	2974.15	76.45	0.14	2.41	15.45	0.17	0.10	1.85	97.51

4.2. Model Construction

After identifying the curves involved in model construction, it is crucial to normalize the data to eliminate dimensional differences among various features. Normalization ensures that the values of different features are compared on the same scale, preventing undue influence from individual features, and promoting model robustness. Moreover, it expedites the convergence process of the model, enhancing training speed and effectiveness.

The normalization technique employed in this study is the Min-Max scaling method, as detailed in Equation (10).

$$x_{i,j}^{*} = \frac{x_{i,j} - x_j^{\min}}{x_j^{\max} - x_j^{\min}} \tag{10}$$

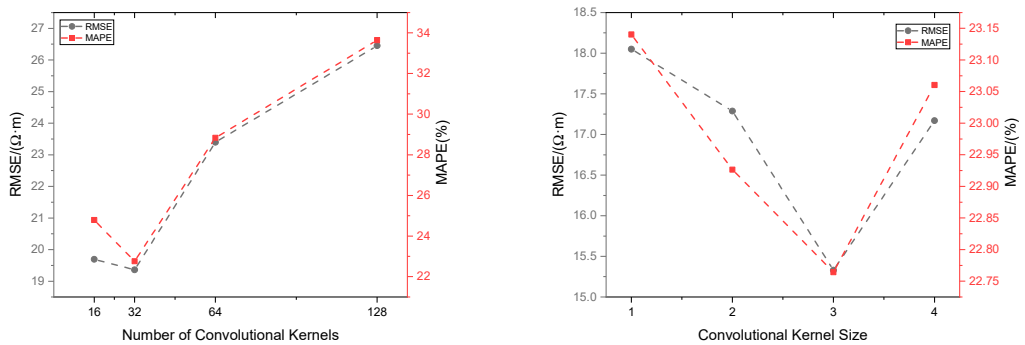
In Equation (10), $x_j^{\min}$ and $x_j^{\max}$ correspond to the minimum and maximum values of $x_{i,j}$ (curves), respectively.

The dataset is divided into training and validation sets in an 8:2 ratio. Hyperparameters for the CNN-GRU-ATT method are then determined, crucial for its predictive performance. These parameters include the width of the convolutional layer scanning window, the number and size of CNN convolutional kernels, the number of GRU neurons, and batch size. Following established practices, common values are considered, such as scanning window widths of 16, 32, 64, and 128, and batch sizes of 32, 64, or 128. The Adam optimizer, proposed by Kingma and Ba [43], is utilized for training neural networks. This optimization method dynamically adjusts the learning rate, combining the benefits of gradient descent and momentum optimization to expedite convergence [42]. Hyperparameters are determined using grid search, evaluating performance based on the Mean Squared Error (MSE) loss function, as defined in Equation (11). A smaller MSE signifies better alignment between model predictions and observed values, indicating higher prediction accuracy.

$$MSE = \frac{\sum_{i=1}^{N} (y_i - \hat{y}_i)^2}{N} \tag{11}$$

In Equation (11), y_i represents the actual measured resistivity value, $\Omega \cdot m$; $\hat{y}_i$ represents the predicted resistivity value, $\Omega \cdot m$; and N denotes the number of samples.

For hyperparameter selection, we first referred to the parameter ranges used in previous studies on well-logging curve reconstruction. Initial testing was conducted using the control variable method and 3-fold cross-validation, where one variable was adjusted at a time to validate the chosen parameter ranges. Figure 11a shows the validation results for the number of CNN convolution kernels, with the lowest error observed at 32 kernels. The optimal kernel size, shown in Figure 11b, was 3×3, yielding the lowest error. After confirming the parameter ranges, we further refined the hyperparameter selection using cross-validation combined with grid search.



(**a**) (**b**)

Figure 11. Partial hyperparameter validation results: (**a**) number of convolutional kernels; (**b**) convolutional kernel size.

Table 3 presents the model architecture, which includes 32 CNN convolutional kernels with a kernel size of 3. To improve model generalization and reduce overfitting, a dropout rate of 0.3 is applied. The two GRU layers consist of 10 and 20 hidden neurons, respectively. Additionally, Figure 12 depicts the loss function plots for both the training

and testing datasets. The loss functions for both datasets converge normally under the model architecture described in Table 3.

Table 3. CNN-GRU-ATT network model architecture.

Layer	Parameters	Value
CNN Layer	Number of Convolutional Kernels	32
	Convolutional Kernel Size	3×3
	Activation Function of Convolutional Layer	ReLu
	Padding Method of Convolutional Layer	Valid
	Pooling Layer Pooling Window Size	2×2
	Pooling Layer Activation Function	ReLu
	Dropout Rate	0.3
GRU Layer	Number of Hidden Neurons U_1	10
	Number of Hidden Neurons U_2	20
Attention	Dimensionality	50
Output Layer (Fully Connected Layer)	Dense1	10
	Dense2	1

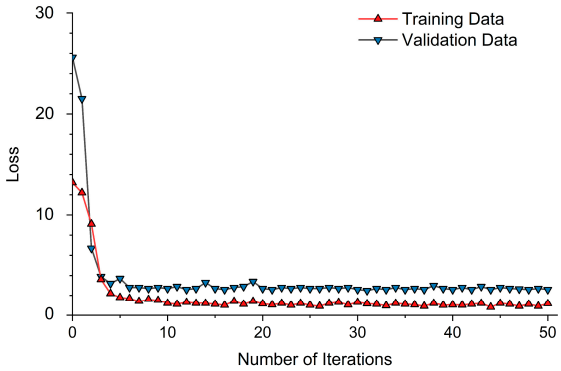


Figure 12. Training and validation dataset loss function plots (red line with red positive triangles for training set data, blue line with blue inverted triangles for validation set data).

4.3. Results and Generalization Verification

Figure 13a depicts the back-testing results of the training dataset, comprising 16,831 data points, demonstrating a significant correlation between predicted and actual values with a coefficient of determination (R^2) of 0.97, indicating excellent model fitting. The mean absolute error (MAE) is recorded at 7.04, with a mean absolute percentage error (MAPE) of 14.19%. Figure 13b showcases the application results on the validation dataset, which consists of 3914 data points. The R^2 between predicted and actual values stands at 0.95, affirming strong predictive capability. Additionally, the MAE for the validation dataset is 6.79, with a MAPE of 17.07%. The consistent error levels across both datasets underscore the robust predictive performance of the model. While slightly higher predictive accuracy is observed for resistivity responses below 10 in the training dataset, effective predictions are maintained across other response ranges, validating the model's correctness.

To ensure model correctness and assess its generalization, two validation methods were employed, firstly, by adjusting the proportion of training data while maintaining the model architecture, ranging from 0.1 to 0.85, and corresponding changes in validation data from 0.9 to 0.15. Testing was conducted on 2000 data groups not used in model construction, measuring Root Mean Square Error (RMSE), MAE, and R^2 (Figure 14). Results revealed a gradual decrease and stabilization of errors with increasing training data, reaching optimal generalization at a training data proportion of 0.65. This research phenomenon indicates that for the inversion of deep resistivity in oil layers, within the same sample space, models constructed with a training data proportion greater than 0.65 have good generalization,

indicating that the training samples involved in model construction cover the entire range of data.

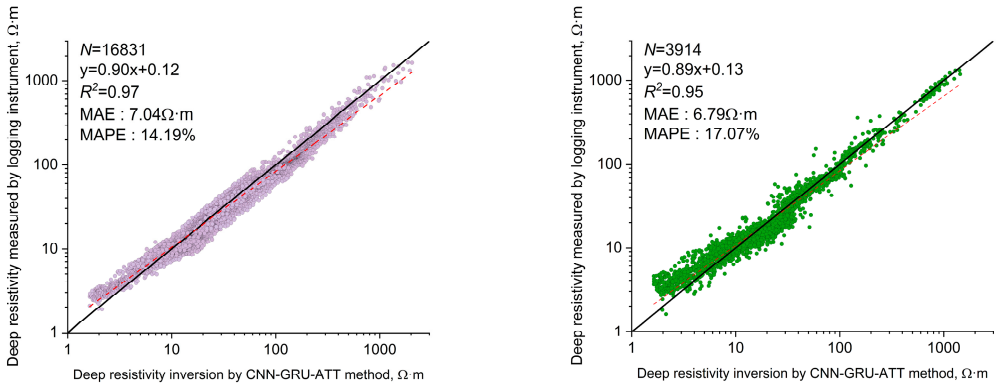


Figure 13. Comparison of model performance between training and validation datasets: (**a**) training set data; (**b**) validation set data.

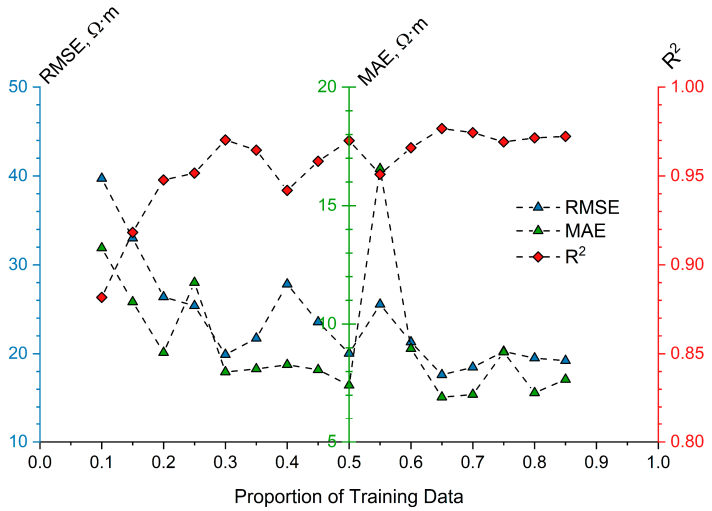


Figure 14. Effectiveness of models constructed with different ratios of training data to validation data on test data not involved in model construction.

For the second point, the constructed model is applied to well M-05X, which was not involved in model construction. Logging curves were collected after drilling in 2013 and production began in early 2014. The three perforation intervals of the well are located between layers MB1_2B and MB2_1. The application effect of the oil layer deep resistivity inversion model to well M-05X is shown in Figure 15a. The sixth track in Figure 15a is the comparison trace, showing the inverted resistivity curve and the LLD curve measured by the DLL. The seventh track is a schematic diagram of the perforation intervals. Figure 15b shows the production curves of the perforation intervals of the well, with the green line representing daily oil production and the blue line representing water production rate. From the production data, the water production rate of the well has remained below 1% since production began, indicating a stable oil layer. Figure 15c shows the intersection diagram of the inverted deep resistivity and the measured LLD. This well M-05X, which was put into production in 2014, experienced unstable oil production rates and was shut down at the end of January 2016. After undergoing hydraulic fracturing, the well resumed production. From the production data, the water cut has remained below 1%, and the perforated section consists entirely of oil-bearing formation. Based on the reconstructed resistivity curve model presented in this paper, the training dataset is composed of the

logging curve responses from the pure oil-bearing section. For the oil-bearing formation, the reconstructed resistivity curve should align with the actual measured deep resistivity curve. In Figure 15a, the trend in the sixth trace shows good agreement with the response, which corresponds to Figure 15c. The inversion results indicate that this section is indeed a pure oil-bearing formation, which is consistent with the production conclusions. This further validates the effectiveness of the constructed model.

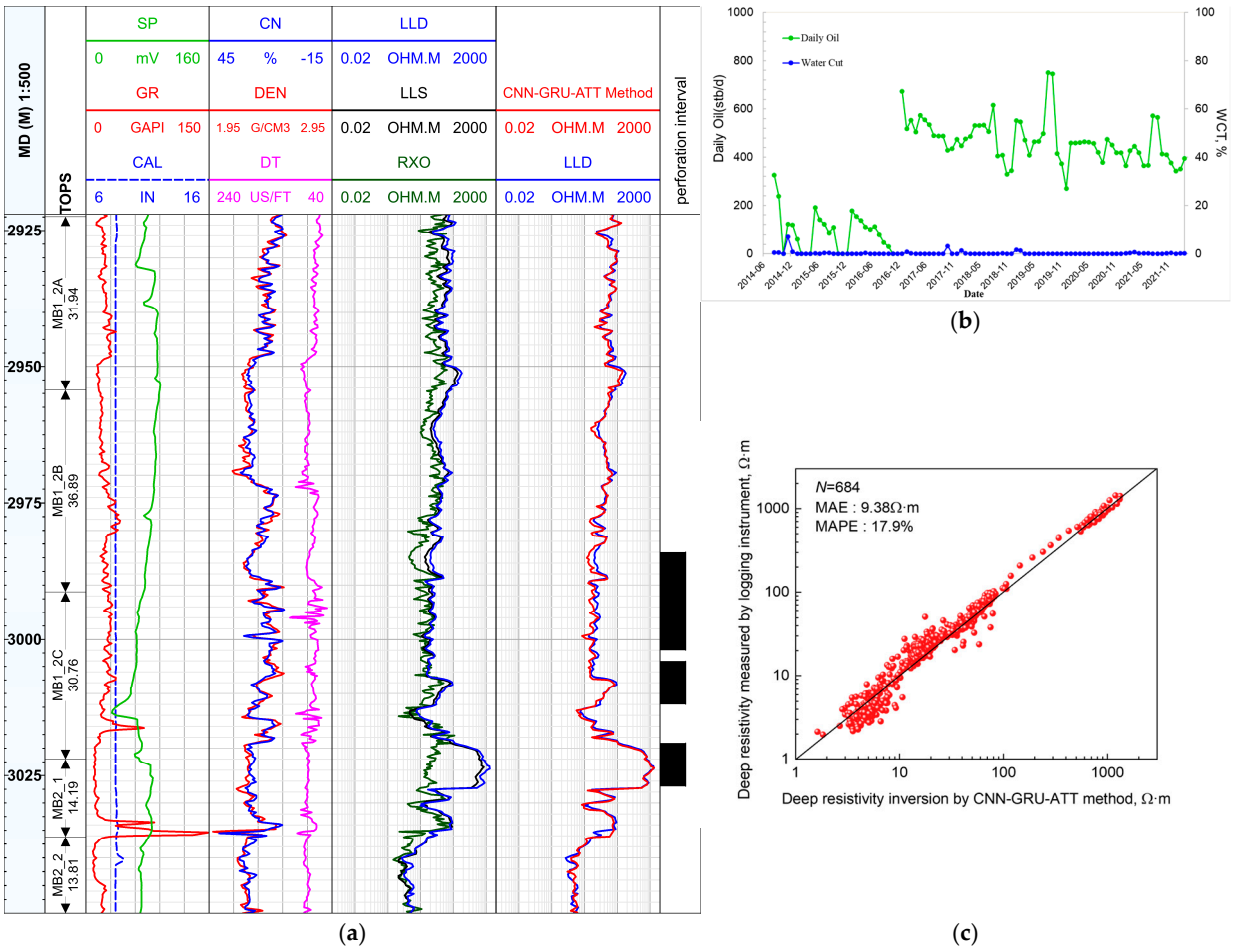


Figure 15. Effectiveness of the constructed CNN-GRU-ATT model in the new well: (**a**) logging and calculation curves of M-05X; (**b**) production data of the shot hole section of well M-05X; (**c**) rendezvous plot of the inverted deep resistivity of the formation section with the instrumental measurements.

In summary, by changing the proportion of training data and blind well application, it is demonstrated that the training data samples involved in model construction are sufficient, and the application effect of the blind well is good, verifying the effectiveness of the method.

5. Applications and Discussion

5.1. Applications

After establishing the inversion model for RD curves in oil reservoirs, the fluid properties can be inferred by comparing the inverted deep resistivity of the oil layer with the actual measured resistivity. In the presence of water in the reservoir, the deep resistivity tends to decrease due to the higher conductivity of water. Therefore, Equation (12) can be utilized for judgment:

$$\Delta R = Inversion_RD - LLD(RLA5) \quad (12)$$

Inversion_RD in Equation (12) is the RD curve for the inverse performance of the method in this paper. After constructing the inversion model for deep resistivity curves in oil reservoirs, the fluid properties can be inferred by comparing the inverted RD with the actual measured resistivity. When the inversion result is greater than the measured result, $\Delta R > 0$, it indicates that the reservoir contains water, and the sampling point depth corresponds to the Oil-Down-To (ODT). Additionally, the Water-Up-To (WUT) can be determined based on the relative positions of the measured and inverted results when the measured resistivity is stable and ΔR is relatively stable.

To conduct these determinations, we utilized two wells for comparison: M-X74 and M-137, as depicted in Figure 16a,b, respectively. In both sets of figures, the fifth track represents the porosity log for identifying reservoir intervals, while the sixth track displays the resistivity log with curves at various depths. The seventh track indicates the inverted deep resistivity and actual deep resistivity logging curves, with fill colors highlighting water-bearing zones where the inversion result exceeds the measured result. The eighth track presents interpretation conclusions, and the ninth track shows perforation intervals.

Figure 16c,d illustrate the production curves of the two wells. The M-X74 well was drilled, completed in 2016, and commenced production in April 2017. Initially, it exhibited high production rates which gradually declined as water production increased over a year. Interpretation suggests that the perforation interval at 3325 m is adjacent to the transition zone (TZ). When the model was applied to this well, the logging data indicated that the reservoir below 3325 m is a water-bearing zone. Specifically, the actual deep resistivity curve of the reservoir below 3325 m is lower than the inversion result, indicating that the reservoir is no longer a pure oil layer. Based on the production data from the perforated section, the water cut has continuously increased over time, suggesting a bottom water breakthrough and that the reservoir has become water-saturated. However, the logging curves reflect static data at the time of logging, and their response is only related to the logging time, without extension over time. Through a back-calculation, the interpretation results align with the actual production data. In the M-137 well, the perforation interval of MB1_2C penetrated the transition zone, resulting in initially high-water production rates followed by a continuous increase. Interpretation conclusions align with production data, confirming the feasibility of identifying reservoir fluid properties using the method based on reconstructing deep resistivity curves in oil layers.

In the study area, the method was applied and compared with production conclusions, test results, and boundary test conclusions, resulting in a confusion matrix (Table 4). The overall application accuracy reached 93.14%. Among 56 oil layers, 54 were effectively identified, with an identification accuracy of 87.5% for transition zone layers. Out of 14 water layers, 13 were correctly identified. For oil layers, there may be misjudgments where the inversion results for oil layer segments are slightly higher than the actual measurements, and the filling area does not gradually increase (as seen near the 3310 m section in Figure 16a). These fall under method misjudgments, which do not adversely affect production.

Table 4. Comparative confusion matrix: methodology application vs. production, oil test, and boundary results.

Accurate Rate (93.14%)	**Prediction Results of the Paper Method**		
Test Results	**Oil or Poor**	**Transition Zone**	**Water**
Oil or Poor	54 (96.43%)	2 (3.57%)	0 (0.00%)
Transition Zone	3 (9.38%)	28 (87.5%)	1 (3.12%)
Water	0 (0.00%)	1 (7.14%)	13 (92.86%)

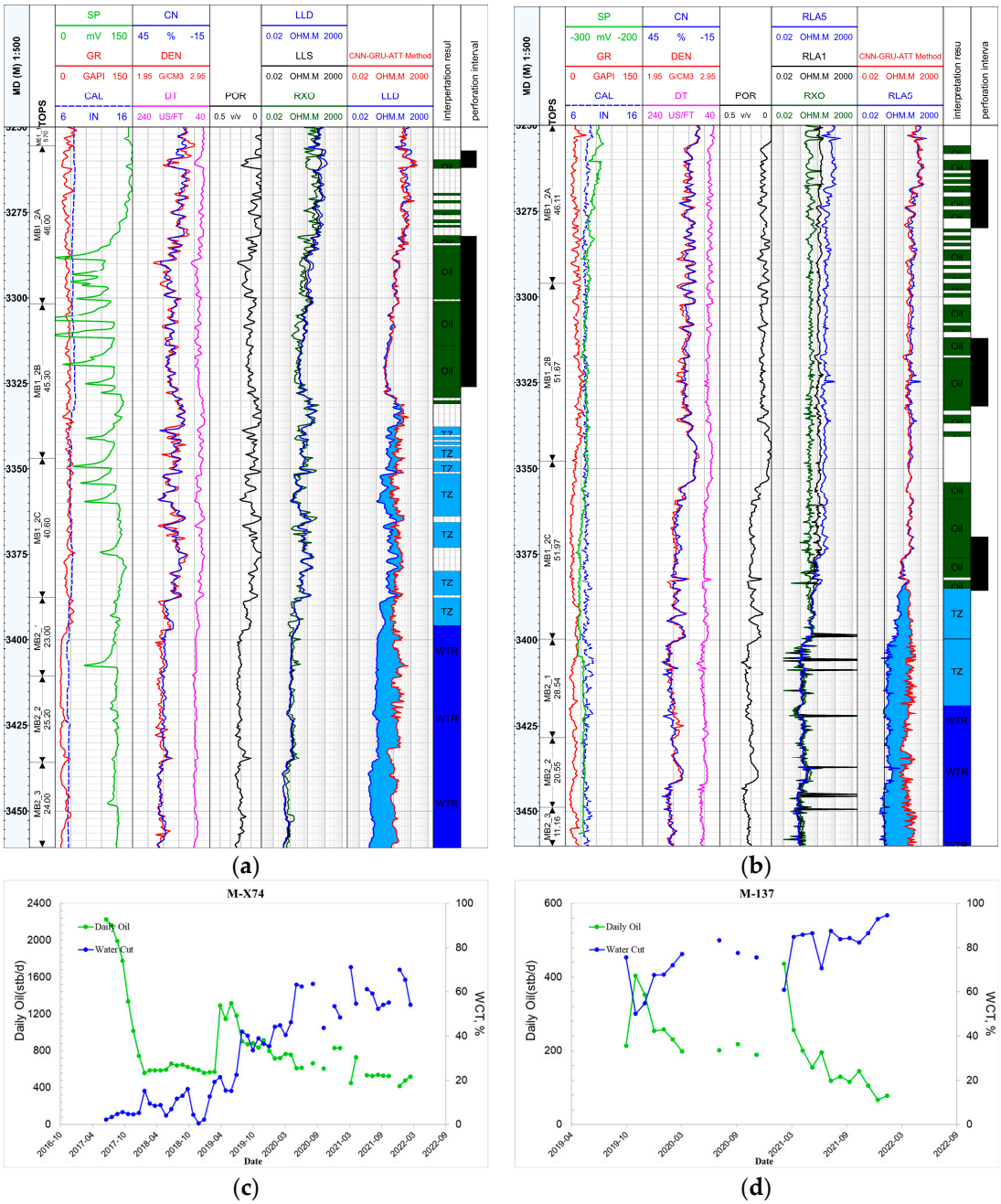


Figure 16. Effectiveness of CNN-GRU-ATT method for practical application in reservoir resistivity inversion: (**a**) logging curve and application effect of well M-X74 using the CNN-GRU-ATT method for reservoir resistivity inversion; (**b**) logging curve and application effect of well M-137 using the CNN-GRU-ATT method for reservoir resistivity inversion; (**c**) production curve of well M-X74; (**d**) production curve of well M-137.

The application of this method to the study area, targeting wells that have not been utilized (original oil well), provides the original ODT and WUT for the block (Figure 17a,b). The results indicate that the range of oil bottom is from 3030 to 3060 m (TVDSS), showing shallower in the southeast and central parts, and deeper in the western, northwestern, and peripheral areas. The range of water top is from 3040 to 3090 m, shallower in the southeast and central parts, and deeper in the northwestern and peripheral areas. The average oil bottom of the original reservoir is 3045 m, and the average water top is 3070 m.

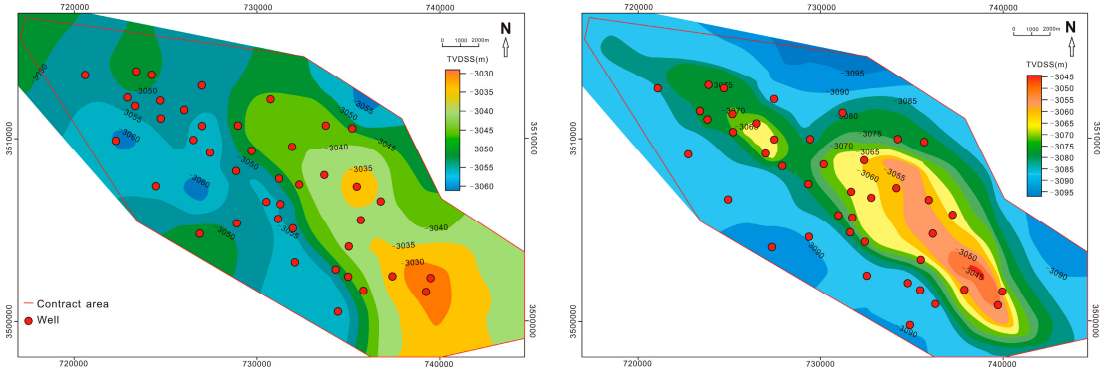


Figure 17. The oil–water interface calculated based on the application of the method of this paper to the original well: (**a**) raw ODT; (**b**) raw WUT.

Simultaneously, a set of well oil–water profiles is presented. Figure 18a corresponds to the MA interval reservoirs, where wells located in high positions correspond to oil layers, while those in low positions reach the transition zone of the MA2 formation. Figure 18b indicates that the oil bottom of the well group is mostly around 3050 m, and as the boreholes vary in position, the ODT and WUT change. Additionally, differences in reservoir properties among different wells can also lead to variations in the length of the transition zone.

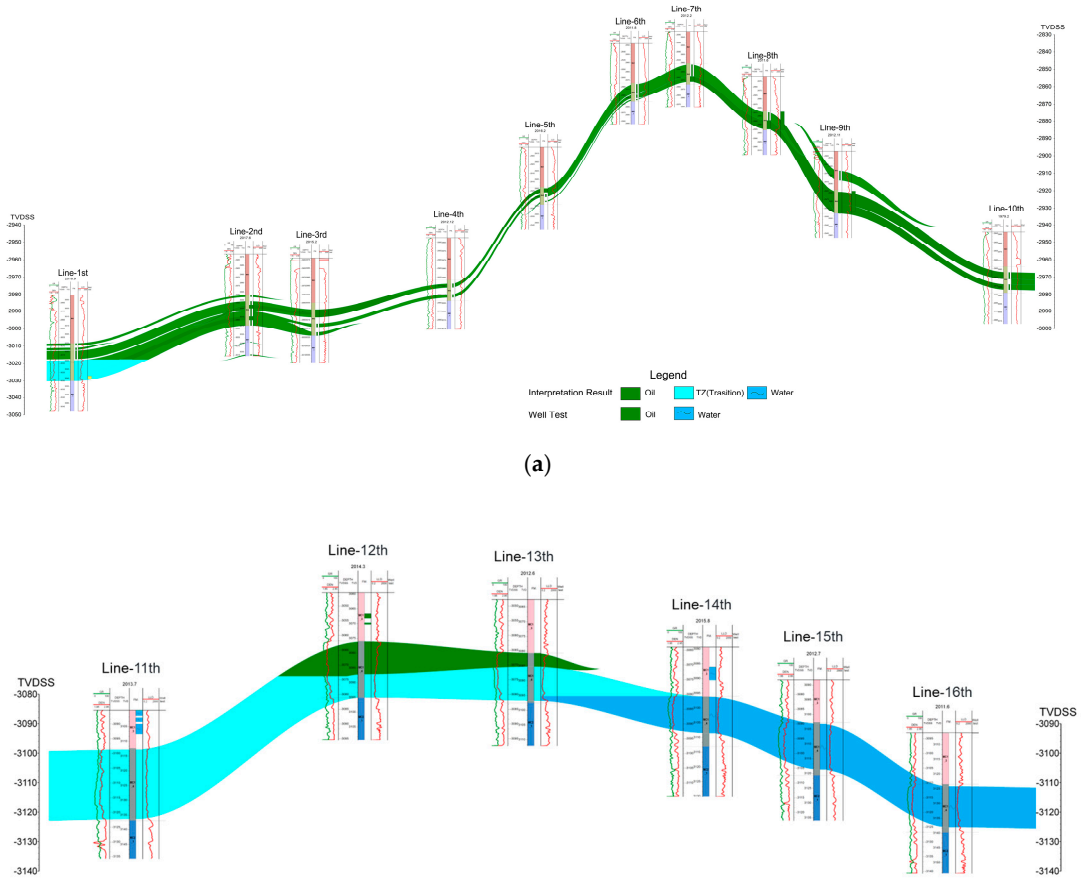


Figure 18. Oil–water profiles calculated based on the methodology of this paper: (**a**) MA reservoir; (**b**) MB-MC reservoir.

5.2. Discussion

5.2.1. Feasibility of Resistivity Inversion

In prior investigations, the focus of logging curve reconstruction was primarily directed towards porosity series logging curves or the recreation of shear wave travel time profiles when array acoustic data were unavailable. Studies conducted by Zhai et al. [44] emphasized that the precision of reconstructing resistivity curves is comparatively lower than that of sonic travel time logging curves and compensated density logging curves. During the reconstruction of resistivity curves, the feature vectors (logging curves) employed for model assembly predominantly underscore the reservoir characteristics. Alterations in fluid properties, such as the transition from an oil layer to a water layer, lead to an escalation in fluid density, which theoretically impacts the logging curve response. This is contingent on the density variance between the reservoir oil and the formation water. Reservoir resistivity curves exhibit a remarkable sensitivity to reservoir fluid properties; the introduction of formation water can prompt a swift decline in reservoir resistivity, with a reduction scale of potentially two orders of magnitude. Nevertheless, alterations in porosity series curves and their derived parameters may not provoke remarkable changes, thereby escalating the challenge in developing profound resistivity curves through traditional methodologies. Furthermore, it is noteworthy that within the study area, the reservoir might contain heavy oil, characterized by high density and a marginal density contrast relative to formation water. Consequently, the resemblance in density attributes between heavy oil and formation water in the reservoir yields insignificant variations in logging response and compromises the accuracy of the resulting resistivity inversion model.

To circumvent the issues, only using data from oil layers as training data can be effective. Assuming that all fluids in the reservoir are oil, a significant decrease in resistivity occurs when the reservoir contains water. When there is a clear difference between the measured curve and the inversion curve, it can be determined that the reservoir contains water.

5.2.2. The Accuracy Advantage of CNN-GRU-ATT Method

In the constructed method for deep resistivity curve inversion of oil layers, this study built a CNN-GRU-ATT network model. To further characterize the application advantages of this model, this study compared the application effects of different network models. Using the same set of training samples and validation data, multiple regression, CNN-GRU model, GRU model, LSTM model, Multiple Regression model, and Random Forest model were constructed for resistivity inversion of oil layers, and the models were applied to the blind well M-05X well (Figure 19). Figure 19a shows the results of the method proposed in this study, constructed by the CNN-GRU-ATT network model. Figure 19b shows the application results of the CNN-GRU method, while Figure 19c–f correspond to the GRU network, LSTM network, Multiple Regression model, and Random Forest model, respectively. To ensure the fairness of model comparison, for all deep learning networks, the hyperparameters are obtained based on grid search with 3-fold cross-validation, and it should also be noted that the coefficients of multiple regression are obtained by fitting the modeled data, and Random Forest, as a machine learning algorithm, also uses grid search with 3-fold cross-validation. Combining Figure 19 indicates that the method proposed in this study and the CNN-GRU model accurately predict the resistivity of layers at and above 3030 m, consistent with the measurement results. However, other methods fail to accurately predict high resistivity values segments, but their application effects are poor when dealing with resistivity segments at and below 3040 m. The application results of the Multiple Regression method indicate that this method has poor anti-interference ability, low accuracy, and is prone to outliers. Meanwhile, the results of the Random Forest method

do not show a trend with the measured results. Regardless of whether the resistivity of the oil layer is high or low, the predicted results fluctuate within a certain range, possibly due to overfitting of the model. Figure 20 plots the error waterfall of each method, and the results show that the proposed method has the lowest RMSE, MAPE, and MAE, which reflects the advantages of the method in this paper [45].

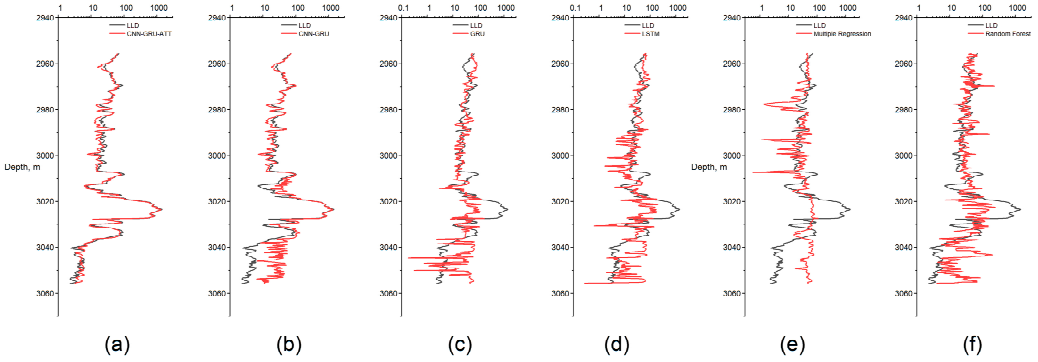


Figure 19. Comparison of the effectiveness of different methods for constructing models based on the same data in the new well: (**a**) CNN-GRU-ATT; (**b**) CNN-GRU; (**c**) GRU; (**d**) LSTM; (**e**) Multiple Regression; (**f**) Random Forest.

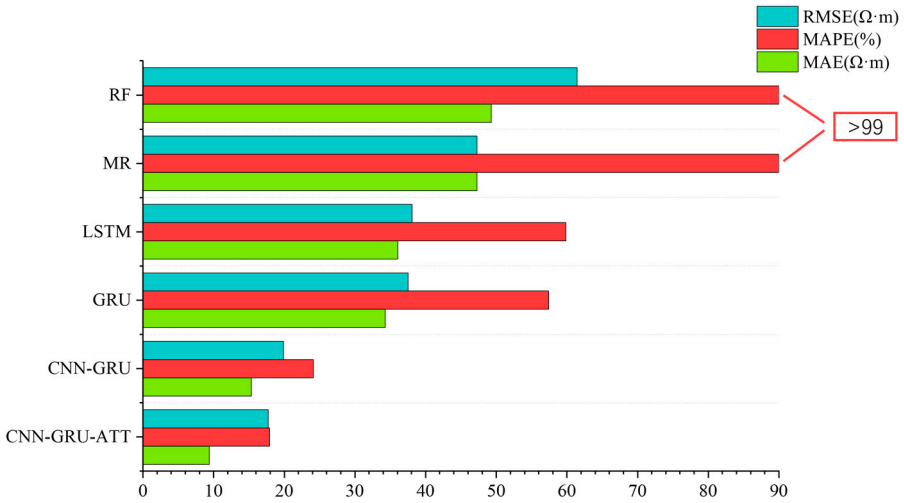


Figure 20. Error waterfall plot for different methods.

Table 5 presents the application evaluation indicators of each method. The errors of the CNN-GRU-ATT network are the lowest, and the fitting degree of the predicted results with the measured results is the highest, followed by the CNN-GRU method. Meanwhile, the average relative error of some methods exceeds 99%, which is because the predicted results are much higher than the measured results in layers at and below 3040 m, resulting in excessively large absolute and relative errors.

Table 5. Error indicators for different methods.

Method n **= 643**	**MAE** Ω·*m*	**MAPE** %	**RMSE** Ω·*m*	**R^2** None
CNN-GRU-ATT	9.38	17.90	17.72	0.92
CNN-GRU	15.34	24.09	19.88	0.84
GRU	34.28	57.40	37.52	0.26
LSTM	36.04	59.83	38.07	0.30
MR	47.29	>99	47.26	<0.10
RF	49.30	>99	61.43	<0.10

In summary, the comparison shows that the CNN-GRU-ATT model network has higher prediction accuracy and is more suitable for constructing deep resistivity curve inversion models of oil layers.

5.2.3. Limitations

In addressing the limitations of this study, three aspects are discussed:

1. Limitations in the selection of training samples: When selecting data to construct the inversion model for oil layer resistivity curves, it is crucial to choose samples from wells with short intervals between drilling and logging. Research by Zhao et al. [25] suggests that reservoirs may be affected by invasion of drilling mud filtrate. Numerical simulations show that with increasing invasion time, the invasion depth also increases, and the invasion rate is correlated with reservoir porosity. Although deep resistivity curves detected by different instruments may have slight differences, it is advisable to avoid selecting well samples with intervals exceeding 15 days between drilling and logging to mitigate errors caused by mud invasion. Additionally, the proposed method can be applied to reconstruct resistivity curves for oil layers in older wells where invasion phenomena are more severe.

For model uncertainty, future improvements can be made to further enhance the reliability of the algorithm by introducing uncertainty quantification techniques. Specifically, a more accurate algorithm can be used to clarify the actual weight of each curve in the model construction, and thus better assess the impact of logging quality on model uncertainty. However, the discussion of uncertainty still needs to be analyzed in depth in relation to the actual situation of specific workings. Clarifying the weights of different curves in resistivity curve reconstruction can help us assess the impact of the acquisition quality of conventional logging curves on model construction and provide clear quantitative indicators for this purpose. Meanwhile, a more comprehensive validity analysis combined with production data and test results will help to further optimize the accuracy and practicality of the model.

2. Sources of errors: The CNN-GRU-ATT network model employed in this study also has inherent errors. Geophysical logging data collection is susceptible to on-site disturbances during operations and variations between different logging instruments. Despite preprocessing steps such as logging standardization, it is challenging to completely eliminate noise. These errors cannot be individually considered, and thus noise models for removal cannot be constructed. Consequently, the model results may contain such noise errors. However, through practical studies, these errors can be manually mitigated. For example, some oil layer segments may exhibit deep resistivity inversion results higher than actual resistivity, but these "spike-like" fillings do not affect the identification of reservoir fluid properties.
3. Limitations in application: The model proposed in this paper demonstrates strong practicality when applied to reservoirs within the same work area and geological background. By collecting deep resistivity curves and other conventional logging data, the model can be directly applied to on-site data processing. The paper also presents test results based on well-log cross-sections, proving the model's effectiveness in practical applications. However, when applied to different work areas, it is crucial to consider the richness and response characteristics of the actual logging data. For reservoirs in different work areas, a new model must be constructed based on the actual data, following the process outlined in this paper. This is particularly important in the case of oil-based mud wells, where we do not recommend using the model, as the properties of oil-based mud wells may lead to a decline in model prediction performance. From a computational cost perspective, deep learning architectures (such as CNN, GRU, and attention mechanisms) inherently involve high computational load,

and their complex interactions may pose challenges for real-time applications. Given the variations in work areas and data quality, it is crucial to assess whether further model optimization is necessary. Nevertheless, for real-time applications, this paper suggests considering the following optimization strategies: first, model compression techniques (such as pruning and quantization) can significantly reduce the computational load, improving real-time inference efficiency. Second, hardware acceleration (e.g., GPU or FPGA) can further optimize the speed of model inference. Additionally, developing a lightweight version of the model can achieve faster inference responses while maintaining adequate accuracy.

Furthermore, the method for identifying reservoir fluid properties proposed in this study has a limited timeframe. As ODT and WUT are continuously changing during production development, the results calculated from logging data correspond to the moment of data collection. This method remains effective in cases where the formation is invaded by edge water and bottom water, such as in a water-flooded reservoir. However, it is important to note that the method becomes inapplicable when the reservoir is flooded by injected water with different salinity compared to the formation water.

6. Conclusions

This study proposes a new method and workflow for deep resistivity curve inversion, yielding the following conclusions:

(1) By employing pure oil layer logging response data as samples and utilizing the CNN-GRU-ATT method, this study successfully constructs deep resistivity curves for oil layers. Compared to other models such as CNN-GRU, GRU, LSTM, Multiple Regression, and Random Forest models, this method significantly improves model accuracy.

(2) Comparing the constructed oil layer deep resistivity curves with the LLD curves (or RLA5 curves) collected by actual logging instruments, it is found that the relative positions of the two can effectively determine the type of reservoir fluid properties. Verified with an accuracy rate of 93.14%, the method aligns with production and well testing conclusions.

(3) Through analysis of the original oil bottom and water top ranges in the study area, certain geographic distribution patterns are observed.

In conclusion, the new method proposed in this study can be applied not only for deep resistivity inversion of oil layers but also for identifying reservoir fluid properties. It has demonstrated good application effectiveness, providing a new approach for on-site reservoir fluid property identification.

Author Contributions: Conceptualization, J.G., Z.Z. (Zhansong Zhang) and H.L.; methodology, J.G., Z.Z. (Zuomin Zhu), Q.Z. and Z.Z. (Zhansong Zhang); software, J.G. and Z.Z. (Zuomin Zhu); validation, J.G., Y.Y. and H.L.; formal analysis, Q.Z. and Y.Y; investigation, Q.Z. and J.G.; resources, J.G. and Z.Z. (Zhansong Zhang); data curation, J.G. and Z.Z. (Zuomin Zhu); writing—original draft preparation, J.G. and Q.Z.; writing—review and editing, J.G. and Y.Y.; visualization, J.G.; supervision, H.L.; project administration, Z.Z. (Zhansong Zhang); funding acquisition, J.G. All authors have read and agreed to the published version of the manuscript.

Funding: This work was financially sponsored by the Open Fund of the Key Laboratory of Exploration, Technologies for Oil and Gas Resources, Ministry of Education (No. K2023-02).

Institutional Review Board Statement: Not applicable.

Informed Consent Statement: Not applicable.

Data Availability Statement: All our data are displayed in the pictures in this paper.

Acknowledgments: The authors would like to express their most sincere gratitude to the field workers in the Halfaya Field.

Conflicts of Interest: Author Qing Zhao was employed by the company Changqing Oilfield. The remaining authors declare that the research was conducted in the absence of any commercial or financial relationships that could be construed as a potential conflict of interest.

Abbreviations

ALRT	Array Laterolog Resistivity Tool
ATT	Attention Mechanism
BPNN	Back-Propagation Neural Network
BS	Bit diameter
CAL	Caliper
CN	Compensated Neutron
CNN	Convolutional Neural Networks
CTS	Casting thin section
DEN	Compensation Density
DLL	Dual Laterolog Resistivity Tool
DT	Acoustic time difference log
DTS	Shear Wave Slowness
DWT	Discrete Wavelet Transform
GR	Nature gamma
GRU	Gated Recurrent Units
LLD	The deep resistivity curve measured by DLL.
LLS	The shallow resistivity curve measured by DLL.
LSTM	Long Short-Term Memory
MAE	Mean Absolute Error
MAPE	Mean Absolute Percentage Error
MSE	Mean Squared Error
ODT	Oil-Down-To
RD	Deep Resistivity
RLA5	The deep resistivity curve measured by ALRT.
RLA1	The shallow resistivity curve measured by ALRT.
RMSE	Root Mean Square Error
RNN	Recurrent Neural Networks
RXO	Flushed Zone Resistivity
R2	Coefficient of Determination
SEM	Scanning electron microscope
SP	Spontaneous potential
SVR	Support Vector Machine Regression
TZ	Transition Zone
TVDSS	True Vertical Depth Subsea
WUT	Water-Up-To
XGB	eXtreme Gradient Boosting
1DCNN	One-Dimensional Convolutional Neural Networks

References

1. Zhang, D.; Chen, Y.; Meng, J. Synthetic well logs generation via Recurrent Neural Networks. *Pet. Explor. Dev.* **2018**, *45*, 629–639. [CrossRef]
2. Zhou, X.; Zhang, C.; Zhang, Z.; Zhang, R.; Zhu, L.; Zhang, C. A saturation evaluation method in tight gas sandstones based on diagenetic facies. *Mar. Pet. Geol.* **2019**, *107*, 310–325. [CrossRef]
3. Guo, J.; Zhang, Z.; Xiao, H.; Zhang, C.; Zhu, L.; Wang, C. Quantitative interpretation of coal industrial components using a gray system and geophysical logging data: A case study from the Qinshui Basin, China. *Front. Earth Sci.* **2023**, *10*, 1031218. [CrossRef]

4. Zhu, L.; Zhang, C.; Zhang, C.; Zhang, Z.; Zhou, X.; Zhu, B. An improved theoretical nonelectric water saturation method for organic shale reservoirs. *IEEE Access* **2019**, *7*, 51441–51456. [CrossRef]
5. Ba, J.; Cao, H.; Carcione, J.M.; Tang, G.; Yan, X.; Sun, W.; Nie, J. Multiscale rock-physics templates for gas detection in carbonate reservoirs. *J. Appl. Geophys.* **2013**, *93*, 77–82. [CrossRef]
6. Mahbaz, S.; Sardar, H.; Namjouyan, M.; Mirzaahmadian, Y. Optimization of reservoir cut-off parameters: A case study in SW Iran. *Pet. Geosci.* **2011**, *17*, 355–363. [CrossRef]
7. Zhang, M.; Jia, A.; Lei, Z. Inter-well reservoir parameter prediction based on LSTM-Attention network and sedimentary microfacies. *Geoenergy Sci. Eng.* **2024**, *235*, 212723. [CrossRef]
8. Fu, X.; Qin, Y.; Wang, G.; Rudolph, V. Evaluation of coal structure and permeability with the aid of geophysical logging technology. *Fuel* **2009**, *88*, 2278–2285. [CrossRef]
9. Torres-Verdín, C.; Angeles, R.; Sepehrnoori, K.; Elshahawi, H. History matching of multiphase-flow formation-tester measurements acquired with focused-sampling probes in deviated wells. *Petrophysics* **2011**, *52*, 14–31.
10. Zhou, B.; O'Brien, G. Improving coal quality estimation through multiple geophysical log analysis. *Int. J. Coal Geol.* **2016**, *167*, 75–92. [CrossRef]
11. Simoes, V.; Maniar, H.; Abubakar, A.; Zhao, T. Comparative Study of Machine-Learning-Based Methods for Log Prediction. *Petrophysics* **2023**, *64*, 192–212. [CrossRef]
12. Song, T.; Zhu, W.; Chen, Z.; Jin, W.; Song, H.; Fan, L.; Yue, M. A novel well-logging data generation model integrated with random forests and adaptive domain clustering algorithms. *Geoenergy Sci. Eng.* **2023**, *231*, 212381. [CrossRef]
13. Xu, S.; Li, S.; Zou, Z. High-resolution sonic slowness estimation based on the reconstruction of neighboring virtual traces. *Surv. Geophys.* **2024**, *45*, 721–743. [CrossRef]
14. Haritha, D.; Satyavani, N. Borehole Log Reconstruction using ANN: A Case Study from KBH-08, Koyna-Warna Region. *J. Geol. Soc. India* **2023**, *99*, 47–54. [CrossRef]
15. Kuang, L.; Liu, H.; Ren, Y.; Luo, K.; Shi, M.; Su, J.; Li, X. Application and development trend of artificial intelligence in petroleum exploration and development. *Pet. Explor. Dev.* **2021**, *48*, 1–14. [CrossRef]
16. Li, N.; Xu, B.; Wu, H.; Feng, Z.; Li, Y.; Wang, K.; Liu, P. Application status and prospects of artificial intelligence in well logging and formation evaluation. *Acta Pet. Sin.* **2021**, *42*, 508–622. [CrossRef]
17. Zhang, J.; Deng, J.; Tan, Q.; Shi, L. Reconstruction of well logs based on XGBoost. *Oil Geophys. Prospect.* **2022**, *57*, 687–705. [CrossRef]
18. Zhang, H.; Wu, W.; Song, X. Well Logs Reconstruction Based on Deep Learning Technology. *IEEE Geosci. Remote Sens. Lett.* **2024**, *21*, 7501205. [CrossRef]
19. Wang, J.; Cao, J.; You, J. Reconstruction of logging traces based on GRU neural network. *Oil Geophys. Prospect.* **2020**, *55*, 510–520. [CrossRef]
20. Lin, L.; Wei, H.; Wu, T.; Zhang, P.; Zhong, Z.; Li, C. Missing well-log reconstruction using a sequence self-attention deep-learning framework. *Geophysics* **2023**, *88*, 391–410. [CrossRef]
21. Ren, Q.; Zhang, H.; Azevedo, L.; Yu, X.; Zhang, D.; Zhao, X.; Zhu, X.; Hu, X. Reconstruction of Missing Well-Logs Using Facies-Informed Discrete Wavelet Transform and Time Series Regression. *SPE J.* **2023**, *28*, 2946–2963. [CrossRef]
22. Guo, J.; Luo, Y.; Zeng, F.; Wang, R.; Yuan, C.; He, L.; Lu, C. Reconstruction of missing shear wave slowness in shale gas reservoir based on deep learning algorithm. *Geoenergy Sci. Eng.* **2023**, *227*, 211865. [CrossRef]
23. Zhu, L.; Ma, Y.; Cai, J.; Zhang, C.; Wu, S.; Zhou, X. Key factors of marine shale conductivity in southern China—Part II: The influence of pore system and the development direction of shale gas saturation models. *J. Pet. Sci. Eng.* **2022**, *209*, 109516. [CrossRef]
24. Zhu, L.; Wu, S.; Zhang, C.; Misra, S.; Zhou, X.; Cai, J. Characterization of pore electrical conductivity in porous media by weakly conductive and nonconductive pores. *Surv. Geophys.* **2023**, *44*, 877–923. [CrossRef]
25. Zhao, Q.; Guo, J.; Zhang, Z. A method for judging the effectiveness of complex tight gas reservoirs based on geophysical logging data and using the L block of the Ordos Basin as a case study. *Processes* **2023**, *11*, 2195. [CrossRef]
26. Hu, Y.; Yu, X.; Chen, G.; Li, S. Classification of the average capillary pressure function and its application in calculating fluid saturation. *Pet. Explor. Dev.* **2012**, *39*, 778–784. [CrossRef]
27. Zhu, L.; Zhang, C.; Zhang, Z.; Zhou, X. High-precision calculation of gas saturation in organic shale pores using an intelligent fusion algorithm and a multi-mineral model. *Adv. Geo-Energy Res.* **2020**, *4*, 135–151. [CrossRef]
28. Qassamipour, M.; Khodapanah, E.; Tabatabaei-Nezhad, S.A. A comprehensive method for determining net pay in exploration/development wells. *J. Pet. Sci. Eng.* **2021**, *196*, 107849. [CrossRef]
29. Gao, J.; Tian, C.; Zhang, W.; Song, X.; Liu, B. Characteristics and genesis of carbonate reservoir of the Mishrif Formation in the Rumaila oil field, Iraq. *Acta Pet. Sin.* **2013**, *34*, 843–852. [CrossRef]
30. Sun, J.; Wang, K.; Li, W. Development and analysis of logging saturation interpretation models. *Pet. Explor. Dev.* **2008**, *35*, 101.

31. Alsharhan, A.S.; Nairn, A.E.M. A review of the Cretaceous formations in the Arabian Peninsula and Gulf: Part I. Lower Cretaceous (Thamama Group) stratigraphy and paleogeography. *J. Pet. Geol.* **1986**, *9*, 365–391. [CrossRef]
32. Alsharhan, A.S.; Nairn, A.E.M. A review of the ctretaceous formations in the arabian peninsula and gulf: Partii. mid-cretaceous (wasia group) stratigraphy and paleogeography. *J. Pet. Geol.* **1988**, *11*, 89–112. [CrossRef]
33. Sadooni, F.N.; Alsharhan, A.S. Stratigraphy, microfacies, and petroleum potential of the Mauddud Formation (Albian–Cenomanian) in the Arabian Gulf basin. *AAPG Bull.* **2003**, *87*, 1653–1680. [CrossRef]
34. Guo, J.; Ling, Z.; Xu, X.; Zhao, Y.; Yang, C.; Wei, B.; Zhang, Z.; Zhang, C.; Tang, X.; Chen, T.; et al. Saturation Determination and Fluid Identification in Carbonate Rocks Based on Well Logging Data: A Middle Eastern Case Study. *Processes* **2023**, *11*, 1282. [CrossRef]
35. Mei, P.; Li, M.; Zhang, Q.; Li, G.; Song, L. Prediction model of drinking water source quality with potential industrial-agricultural pollution based on CNN-GRU-Attention. *J. Hydorl.* **2022**, *610*, 127934. [CrossRef]
36. Wang, Y.; Sun, Y.; Liu, Z.; Sarma, S.E.; Bronstein, M.M.; Solomon, J.M. Dynamic graph cnn for learning on point clouds. *ACM Trans. Graph. (Tog)* **2019**, *38*, 1–12. [CrossRef]
37. Das, V.; Pollack, A.; Wollner, U.; Mukerji, T. Convolutional neural network for seismic impedance inversion. *Geophysics* **2019**, *84*, 869–880. [CrossRef]
38. Jiao, R.; Huang, X.; Ma, X.; Han, L.; Tian, W. A model combining stacked auto encoder and back propagation algorithm for short-term wind power forecasting. *IEEE Access* **2018**, *6*, 17851–17858. [CrossRef]
39. Chen, T.; Gao, G.; Liu, H.; Li, Y.; Gui, Z.; Yu, Z.; Zhai, X. Rock brittleness index inversion method with constraints of seismic and well logs via a CNN-GRU fusion network based on the spatiotemporal attention mechanism. *Geoenergy Sci. Eng.* **2023**, *225*, 211646. [CrossRef]
40. Hochreiter, S.; Schmidhuber, J. Long short-term memory. *Neural Comput.* **1997**, *9*, 1735–1780. [CrossRef] [PubMed]
41. Shan, L.; Liu, Y.; Tang, M.; Yang, M.; Bai, X. CNN-BiLSTM hybrid neural networks with attention mechanism for well log prediction. *J. Pet. Sci. Eng.* **2021**, *205*, 108838. [CrossRef]
42. Srivastava, N.; Hinton, G.; Krizhevsky, A.; Sutskever, I.; Salakhutdinov, R. Dropout: A simple way to prevent neural networks from overfitting. *J. Mach. Learn. Res.* **2014**, *15*, 1929–1958.
43. Kingma, D.P.; Ba, J. Adam: A method for stochastic optimization. *arXiv* **2014**, arXiv:1412.6980. [CrossRef]
44. Zhai, X.; Gao, G.; Li, Y.; Chen, D.; Gui, Z.; Wang, Z. Reconstruction method of logging curves by 2D convolutional neural network integrating attention mechanism. *Oil Geophys. Prospect.* **2023**, *58*, 1031–1041. [CrossRef]
45. Sharma, A.; Burak, T.; Nygaard, R.; Hoel, E.; Kristiansen, T.; Hellvik, S.; Welmer, M. Projecting Petrophysical Logs at the Bit through Multi-Well Data Analysis with Machine Learning. In Proceedings of the SPE Offshore Europe Conference and Exhibition, Aberdeen, Scotland, UK, 5–8 September 2023; p. D031S012R001. [CrossRef]

Disclaimer/Publisher's Note: The statements, opinions and data contained in all publications are solely those of the individual author(s) and contributor(s) and not of MDPI and/or the editor(s). MDPI and/or the editor(s) disclaim responsibility for any injury to people or property resulting from any ideas, methods, instructions or products referred to in the content.